Energy dissipation via electron energization in standing shear Alfvén waves

P. A. Damiano[a)] and A. N. Wright
Mathematical Institute, University of St. Andrews., St. Andrews, United Kingdom KY16 9SS

R. D. Sydora and J. C. Samson
Department of Physics, University of Alberta, Edmonton, Alberta, Canada T6G2J1

A two-dimensional hybrid magnetohydrodynamic-kinetic electron model in dipolar coordinates is used to study the case of a fundamental mode toroidal field line resonance (FLR) centered on an $L=10$ closed dipolar magnetic field line. The model is initialized via a perturbation of the azimuthal shear Alfvén velocity so that only upward field aligned currents (corresponding to downwelling electrons) are present at the ionospheric boundaries during the first half wave period. It is found that the acceleration of the electrons to carry the field aligned currents can be a significant sink of Alfvén wave energy depending on the width of the flux tube. For a FLR with an equatorial perpendicular wavelength of 0.25 R_E about 20% of the wave energy is dissipated over a half cycle. This varies inversely with the width of the flux tube increasing to 40% by a width of 0.15 R_E, which, unless the system is driven, can completely damp the resonance in about $2-3$ cycles. © *2007 American Institute of Physics*. [DOI: 10.1063/1.2744226]

I. INTRODUCTION

In standing shear Alfvén waves in the Earth's magnetosphere, electrons accelerated to carry field aligned currents of several $\mu A/m^2$ are deposited into the auroral ionosphere to produce visible auroral arcs. This has been well established by both ground based and satellite observations[1–3] but in the single fluid picture, which has been used to study the system quite extensively, $m_e \rightarrow 0$ and the acceleration of electrons has not been considered as a significant drain of Alfvén wave energy. Traditionally, the decay of these standing modes [also known as field line resonances (FLRs)] has been associated with Ohmic heating in the Poynting vector fed ionospheric Pedersen currents.[4–6] However, recent observations from the FAST satellite have illustrated that the electron energy flux can be of similar magnitude to the Poynting flux which feeds the ionospheric currents.[7,8] Additionally, Ref. 9, using a two fluid analysis, illustrated that the dissipation due to electron energization was of similar magnitude. They showed that although the electron mass is small, nonlinear inertial effects were important since electrons move rapidly to carry the required currents ($\sim 10^7$ m/s for $j_{\parallel} \sim \mu A/m^2$).

In this paper, we will revisit this issue using a self-consistent 2D hybrid magnetohydrodynamic (MHD) kinetic electron model in dipolar coordinates to study the electron response to a fundamental mode standing shear Alfvén wave on an $L=10$ magnetic field line. The system is initialized so that we only consider the case of upward field aligned currents corresponding to downwelling electrons during the first half Alfvén period as these are responsible for auroral arc formation. Reference 10 studied the coupling of magnetospheric cavity modes to FLRs and found asymptotic widths from about 0.2 to 0.4 R_E (in good agreement with observa-

tions) depending on coupling strength and field line. Therefore an intermediate value of 0.25 R_E was chosen as a case study but comments will be made on resonance widths from 0.15 to 0.5 R_E.

In recent years, several studies have looked at self-consistent kinetic electron effects in shear Alfvén wave pulses[11–15] and standing shear Alfvén waves[16,17] in a Cartesian geometry, but this is (as far as we are aware), the first model to consider a full standing FLR system in a proper 2D dipolar geometry with self-consistent kinetic electron dynamics. It is a modified version of a model initially developed in Ref. 18.

The rest of the paper is broken up into 3 sections and 3 appendices. Section II summarizes the hybrid model. Section III presents the simulation results and discussion while Sec. IV is a summary. The appendices are devoted to model details with Appendix A summarizing the Particle-In-Cell (PIC) method used for the particle interpolation; Appendix B summarizes the derivation of the parallel electric field expression; and Appendix C discusses the energy continuity.

II. HYBRID MODEL

The model used here is based on the box model described in Ref. 16 but also includes the mirror force which is absent in the Cartesian geometry. However, the basic method of the solution is similar. As in the case of the box model the basis for this model are the cold plasma MHD equations and the guiding center equations for the electron dynamics. Defining the ambient magnetic field to be in the x_1 direction such that $\vec{B}=B_o\hat{x}_1$ (refer to Fig. 1) we consider a toroidal Alfvén mode with zero azimuthal wave number ($\partial/\partial x_3=0$) which incorporates only azimuthal perturbations of shear velocity u_3 and magnetic field b_3. These are described in terms
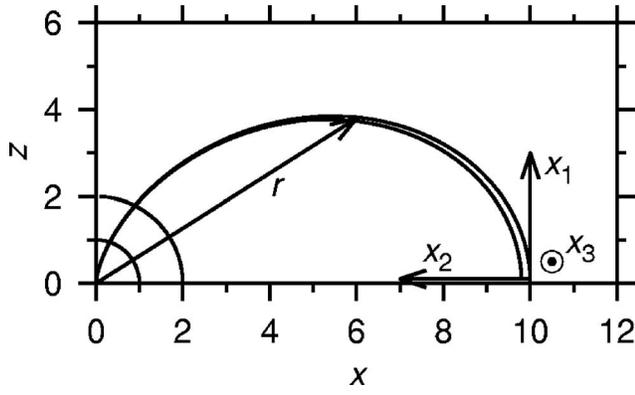
---
a)Electronic mail: pdamiano@mcs.st-and.ac.uk

FIG. 1. Simulation domain in dipolar coordinates (upper half plane only shown) where x_3 is positive increasing out of the page. The circle of radius 2 defines the "ionospheric" boundary in the present simulations. For comparison, the circle of radius 1 defines the Earth's surface. θ is the angle subtended from the z axis.

of the linear cold plasma MHD equations in curvilinear coordinates by

$$\mu_o \rho_o \frac{\partial u_3}{\partial t} = \frac{B_o}{h_1 h_3} \left(\frac{\partial}{\partial x_1} (h_3 b_3) \right), \qquad (1)$$

$$\frac{\partial b_3}{\partial t} = \frac{-1}{h_1 h_2} \left(\frac{\partial}{\partial x_1} (h_2 E_2) - \frac{\partial}{\partial x_2} (h_1 E_1) \right), \qquad (2)$$

where $x_1 = \cos\theta/r^2$, $x_2 = \sin^2\theta/r$ and $x_3 = \phi$ and the dipolar matrics are given in terms of spherical coordinates by $h_1 = r^3/(1+3\cos^2\theta)^{1/2}$, $h_2 = r^2/(\sin\theta(1+3\cos^2\theta)^{1/2})$, and $h_3 = r\sin\theta$. In the limit $m_e \to 0$ ($\omega/\omega_{pe} \ll 1$), $E_1 \equiv 0$ giving Ohm's law as $E_2 = -u_3 B_o$. Incorporating this, Eqs. (1) and (2) are completely self-consistent and describe the massless electron response to ion polarization currents perpendicular to the ambient magnetic field. In what follows, this will be termed the MHD model. The response of the electrons is to move along the ambient magnetic field lines as this is the quickest way for the plasma to maintain quasineutrality. Since the field aligned response of the ions is m_e/m_i slower, to first order the parallel current is assumed to be carried by electrons. The smallest scale that emerges in our simulations is several electron inertial lengths ($\lambda_e = \sqrt{m_e/\mu_o n e^2}$). The electron gyroradius ($r_{ge} = m v_\perp/eB \ll \lambda_e$) is sufficiently small that we employ the guiding center approximation for electrons, which, including the mirror force, is given by

$$m_e \frac{dv_1}{dt} = -eE_1 - \mu_m \frac{1}{h_1} \frac{\partial B_o}{\partial x_1}, \qquad (3)$$

$$h_1 \frac{dx_1}{dt} = v_1. \qquad (4)$$

Here v_1 is the parallel velocity component and x_1 is the position of the electron guiding center, whilst μ_m is the magnetic moment. In advancing the electrons using (3) and (4), the metrics must be calculated using r and θ. This is done solving for the real root of the polynomial $x_1^2 r^4 + r x_2 = 1$ (derived from the definitions of x_1 and x_2) to get r and using the definition of x_1 to determine θ.

The closure between the fluid and electrons is obtained via the parallel electric field described by a variant of the generalized Ohm's law incorporating mirror force effects (see Appendix B) denoted by

$$\frac{\partial}{\partial x_2} \left(\frac{h_3}{h_1 h_2} \left(\frac{\partial G}{\partial x_2} \right) \right) - \frac{G}{\lambda_e^2}$$
$$= \frac{\partial}{\partial x_2} \left(\frac{h_3}{h_1 h_2} \frac{\partial}{\partial x_1} (h_2 E_2) \right) + e\mu_o \frac{\partial}{\partial x_1} \int v_1^2 f d^3 v$$
$$+ \mu_o \frac{e}{m_e} \frac{\partial B_o}{\partial x_1} \int \mu_m f d^3 v - 2\mu_o \frac{e}{m_e} \frac{\partial B_o}{\partial x_1} \int \frac{m_e v_1^2}{2B_o} f d^3 v, \qquad (5)$$

where $G = h_1 E_1$. Once the right-hand side of Eq. (5) is determined, G can be solved for using a tridiagonal solver routine and hence E_1 obtained. The perpendicular electric field E_2 is calculated from the ideal MHD approximation $E_2 = -u_3 B_o$ and the last three terms on the right-hand side are calculated from the electron distribution function.

As discussed in Refs. 16 and 17, the model Eqs. (1)–(4) are advanced in time using a predictor-corrector scheme but this is insufficient to enforce quasineutrality ($\nabla \cdot \vec{j} \approx 0$) since the electron current density is not directly coupled in. Therefore a correction to the perpendicular electric field E_{2c} is determined from the remaining divergence of the current density via the expression

$$\epsilon_o \frac{\partial}{\partial t} \left(\frac{1}{h_1 h_2 h_3} \frac{\partial}{\partial x_2} (h_1 h_3 E_{2c}) \right)$$
$$= -\nabla \cdot \vec{j} = \frac{-1}{h_1 h_2 h_3} \left(\frac{\partial}{\partial x_1} (h_2 h_3 j_e) + \frac{\partial}{\partial x_2} (h_1 h_3 j_2) \right), \quad (6)$$

where $j_e = -e \int v_1 f d^3 v = -e \Sigma_i v_{1_i} S(\vec{x}, \vec{x}_i)$ and $S(\vec{x}, \vec{x}_i)$ is the particle shape function (see Appendix A). Equation (6) is derived from the continuity equations for electrons and ions and Poisson's equation (see Ref. 16 for Cartesian equivalent) or from the consideration of the full Ampere's law (including displacement current, see Ref. 17 for discussion). Once E_{2c} is determined, E_1 is corrected by incorporating E_{2c} in the first term on right-hand side of Eq. (5) at the corrector step. The time integration in (6) is done using an Euler scheme and the spatial integration over x_2 to determine E_{2c} is done using a fourth order Runge-Kutta integration scheme.

The MHD equations are solved on a set dipolar grid with the spatial derivatives calculated using first order centered finite differences. The grid is set up using n_2 positions in x_2 equally spaced in r_o at the equator and n_1 positions in x_1 equally spaced in length along the field line of minimum x_2. The electrons are initialized and are free to move (parallel to **B**) anywhere in the 2D space. Construction of the electron distribution functions at the grid points (and interpolation of the field values at the particle positions) are determined using PIC techniques (see Appendix A). The particle positions are initialized to create a constant number density profile everywhere in the simulation domain and the total particle velocities are assigned using a 1D Maxwellian as a probability distribution function

$$f(v) \propto e^{-m_e v^2 / 2k_B T}, \tag{7}$$

where a thermal temperature of $k_B T = 5$ eV was used. This is significantly colder than the typical plasma temperatures of a keV for the field line under consideration, but we wanted to initially study the system in the absence of significant mirror force effects ($v_{th} < v_d$ where v_d is the drift velocity of the distribution function). Once the total velocities are assigned, the pitch angles ($\alpha = \arctan v_\perp / v_\parallel$) are chosen so that the electron number density is constant on a sphere of radius v in velocity space. This results in a uniform distribution that ensures a balance between the electric field contributions from the perpendicular and parallel electron pressures (in the equilibrium state) yielding no ambient electron currents in the absence of a shear Alfvén wave perturbation. The parallel and perpendicular electron velocities are determined from the pitch angle using $v_1 = v_\parallel = v \cos \alpha$ and $v_\perp = v \sin \alpha$, respectively, and the magnetic moment of each electron is determined from the perpendicular velocity using $\mu_m = 1/2 m_e v_\perp^2 / B_o$ where B_o is the ambient magnetic field value at the particle's position at $t=0$. The motion of all the electrons maintains μ_m as a constant of the motion. Although $v_\perp$ is not evolved it is determined from the magnetic moment in the code as required for energy calculations.

At the ionospheres, perfectly conducting boundary conditions are assumed with a node in u_3 consistent with $u_2 = j_2 = 0$ and antinodes in parallel current and azimuthal magnetic field ($\partial(h_1 j_1)/\partial x_1 = \partial(h_3 b_3)/\partial x_1 = 0$). In the perpendicular direction (i.e., the boundaries at $x_2 = $ constant) a node in current is assumed which requires a node in E_1, an antinode in azimuthal magnetic field ($\partial(h_3 b_3)/\partial x_2 = 0$), perpendicular current density, ($\partial(h_1 h_3 j_2)/\partial x_2 = 0$) and azimuthal velocity $\partial/\partial x_2 (h_1 h_3 u_3 / B_o) = 0$. The initial perturbation applied to the system (see Sec. III) leads to a very steep rise in parallel current at the $L=10$ field line boundary. This results in some problems when the thermal temperature is nonzero and so the particle velocities are multiplied by a hyper-Gaussian function that goes to zero very rapidly as a function of x_2 close to the $L=10$ field line boundary but is unity everywhere else. This serves to minimize the effects at the boundary, but is well away from the resulting current maximum and so does not effect the results presented here. The antinode boundary condition of the field aligned current at the ionospheric boundaries requires that electrons can be lost from the simulation domain when $j_1 \neq 0$. This is imposed on the electrons by defining a critical current density j_c which is determined as an average of the statistical noise in the electron current j_e evident at the right-hand side of the grid where the perturbation goes to zero. If the electron current compiled at the ionospheric grid cell $|j_e| \leq |j_c|$ (j_e is positive or negative depending on the end of the field line one considers) then precipitating electrons within the grid cell are reflected back into the simulation domain. This is the situation at early times, but as the system evolves and $\nabla \times \vec{b}$ increases, the electron distribution drifts such that $|j_e| > |j_c|$, and the electrons are allowed to precipitate. Since we are only considering the situation of upward field aligned currents and most current carrying electrons that reach the boundary would be precipitated (as their mirror point would

be well into the ionosphere), the approximation works well and the quantitative simulation results (smoothness aside) are rather insensitive to the exact particle number. It should be noted that for the hybrid model, j_e implies the parallel current density obtained directly from the electrons and j_1 is from the solution of Ampère's law. They agree well with each other within numerical noise (see Ref. 16 for comparisons) and for all plots in the paper involving the hybrid current we plot j_e directly (even if labelled j_1).

The ionospheric boundary positions for the following simulations were placed at an altitude of 2 R_E (measured from the center of the Earth). This was chosen as other works (i.e. Ref. 19) have shown that most of the acceleration will take place at altitudes above the B/n peak which, depending on parameters, can be at an altitude of 1 R_E (i.e., radial distance of 2 R_E). This is because as density increases into the ionosphere, less distribution function drift (and consequently energy) would be required to carry a given current. If the B/n peak were lower, the acceleration as noted here would be larger and the energy transfer to the electrons enhanced.

In the simulations presented here, a constant plasma number density of $n = 10^6$ m^{-3} (where $\rho_o = n m_p$) was chosen. For an $L=10$ magnetic field line this results in Alfvén speeds of about 7000 km/s at the equator and 1.5×10^5 km/s at the ionospheric boundaries. The simulation grid consists of 128 and 180 points in the x_2 and x_1 directions, respectively, and 64 million simulation particles were used (scaled to match the above density as discussed in Appendix A). The time step was 0.0027 s. All length scales in the model were normalized by $L_N = 1$ R_E, velocities by $V_N = \sqrt{B_N^2/(\mu_o \rho_N)}$, time by $t_N = L_N/V_N$, currents by $j_N = B_N/(\mu_o L_N)$, and electric fields using $E_n = v_N B_N$ where $B_N = 10$ nT and $\rho_N = 10^5$ m^{-3}. The quantities in the figures are plotted in nondimensional units unless the explicit dimensions are given.

III. SIMULATIONS

Field line resonances are the result of the mode conversion from fast magnetoacoustic modes that allow for the growth of the shear Alfvén wave perturbation from zero over several cycles. This involves an interplay of magnetospheric electrons being precipitated into the ionosphere during the upward current phase and ionospheric electrons being accelerated into the magnetosphere during the downward current phase resulting in a complex distribution function that evolves with the magnetic field $\vec{b}$. A full consideration of this is beyond the scope of the present work, in which we focus on understanding the simpler problem of the response of a uniform Maxwellian electron distribution to the shear Alfvén wave perturbation in the upward current part of a FLR. To accomplish this, the initial state for the simulation is chosen to correspond to the phase of the MHD solution when $j_1 = 0$ by using the eigenmode solution for u_3 in the absence of any b_3 perturbation. The zero current condition of the imposed uniform electron distribution function is thus consistent with this. Test simulations (not shown) have demonstrated that the resulting solution is very insensitive to the initial $E_\parallel$ profile. This is attributed to the "corrector" nature
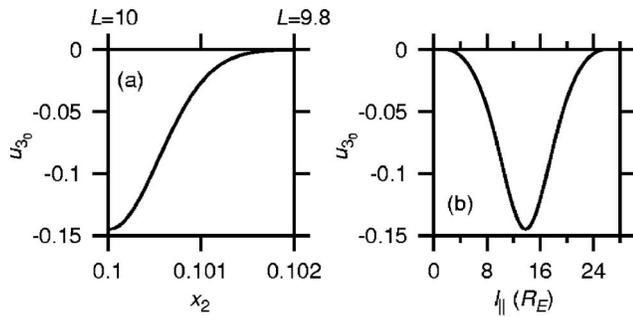
FIG. 2. (a) Azimuthal velocity perturbation as a function of x_2 at the equator ($x_1=0$). (b) Same, but as a function of x_1 (along $x_2=0.1$, i.e., $L=10$).

of the algorithm (see Ref. 17 for discussion) and the fact that $E_\parallel$ only has an observable effect over statistical noise when many time steps are considered (see Sec. III). This was tested by using either $E_\parallel=0$ or $E_\parallel$ defined through Eq. (5) at $t=0$ (and integrating the electrons back a time step consistent with this field to define the initial positions and velocities). The latter is the more correct since it gives $dj_e/dt \neq 0$ at $t=0$ (rather than $dj_e/dt=0$) which is consistent with the standing Alfvén wave we wish to represent. A more complete treatment (in terms of initializing the simulation from a perturbation with zero amplitude) will be the subject of a future investigation.

The standing shear Alfvén wave perturbation used (illustrated in Fig. 2) is given by the expression

$$u_3(x_2,x_1,t_o) = Af(x_1)\exp\left(-\frac{(1/x_2-1/x_{2r})^2}{2\sigma_\perp^2}\right), \qquad (8)$$

where A is the maximum shear velocity at the equator set to 100 km/s and $f(x_1)$ is the approximate eigenfunction solution for a standing shear Alfvén wave along an $L=10$ magnetic field line with a constant density profile. The expression for $f(x_1)$ (which is normalized to unity at the equator) is adapted from Eq. (32) in Ref. 19 and derived from the model of Ref. 20. For a constant density of 10^6 m$_p$ m^{-3}, the period of the standing shear Alfvén mode is about 270 s. For the Gaussian profile in the x_2 direction, x_{2r} is the value at the $L=10$ magnetic field line and the standard deviation, $\sigma_\perp$ is defined such that the full width at half maximum (FWHM) of the Gaussian is equal to $1/2\lambda_{\perp_{eq}}$ ($\sigma_\perp=\lambda_{\perp_{eq}}/(4\sqrt{2\ln 2})$). This choice of perpendicular profile results in only upward field aligned currents at both ionospheric boundaries (corresponding to downwelling electrons) during the first half Alfvén period. For the following calculations, an intermediate value of $\lambda_{\perp_{eq}}=0.25\ R_E$ was chosen.

Figure 3 displays the profiles of parallel current density at the northern ionospheric boundary as a function of x_2 for both the hybrid and MHD models at $t=20$, 50, and 70 s. In order to smooth out the noise, the current values in the hybrid case (dotted line) have been averaged with adjacent grid points (using a weighting of $1/4-1/2-1/4$, see Ref 21 Appendix C) in both the x_1 and x_2 directions with the same being done in the MHD case for consistency. The two models are in good agreement at $t=20$ s, but a small difference is apparent at $t=50$ s which increases further by 70 s. In com-
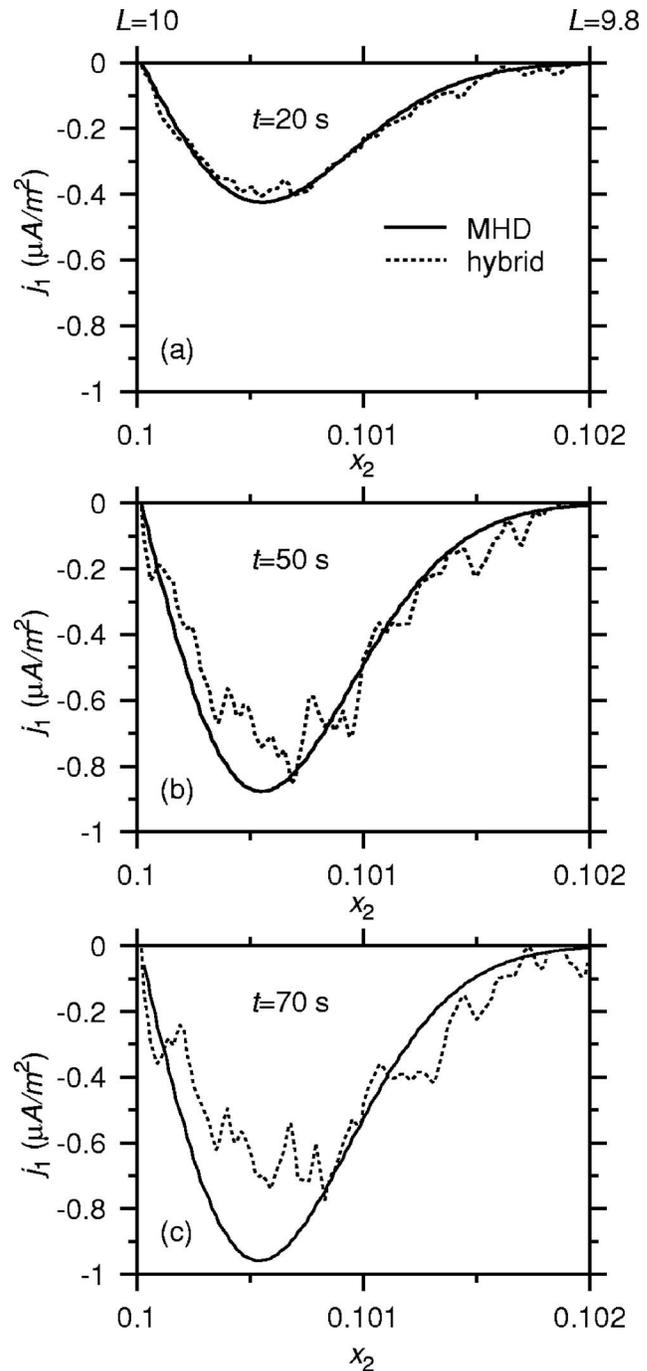

FIG. 3. Parallel current density at the northern ionospheric boundary at $t=20$ s (a), $t=50$ s (b), and $t=70$ s (c).

paring the hybrid current density at these latter two times it is evident that both are more or less saturated at the same level of $\sim 0.7\ \mu\text{A/m}^2$, while the MHD current continues to grow.

Figure 4 displays the evolution of the distribution function in the end ionospheric grid cells between $x_2=0.1005$ and 0.1006 (corresponding to the range of maximum current) binned as a function of $v_\parallel$ alone (irrespective of the value of $v_\perp$). The distribution function drifts more to the right as time progresses to carry the increasing current. The positive displacement is consistent with negative current as in the definition $j_1=-nev_d$ where v_d denotes the mean drift. The mag-
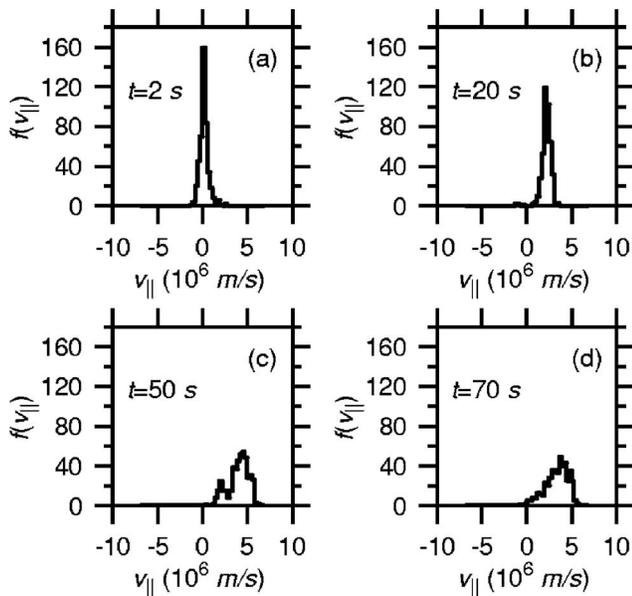
FIG. 4. Distribution function at the northern ionospheric boundary at t = 1 s (a), $t=20$ s (b), $t=50$ s (c), and $t=70$ s (d). Distribution functions are compiled for electrons with radial positions $0.1004 \leqslant x_2 \leqslant 0.1006$ in the last line of grid cells before the ionospheric boundary.

nitude of the drifts seems very similar at $t=50$ and $t=70$ s which is consistent with the saturated current level noted at the same times in Fig. 3. The energy of the electrons at the peak of the distribution function at $t=50$ s is approximately 70 eV. Also evident in these latter two frames of Fig. 4 is what appears to be the formation of a tail behind the drifting bulk of the distribution function. For clarification, the distribution functions at $t=20$ and 70 s are replotted as a function of both $v_\parallel$ and $|v_\perp|$ in Fig. 5. The perpendicular velocity is calculated from the magnetic moment of each electron and so only the absolute value is shown. Besides the drift of the bulk, the distribution function spreads out in the range of parallel and perpendicular velocities and an oblique tail forms which can sometimes extend to slightly negative par-
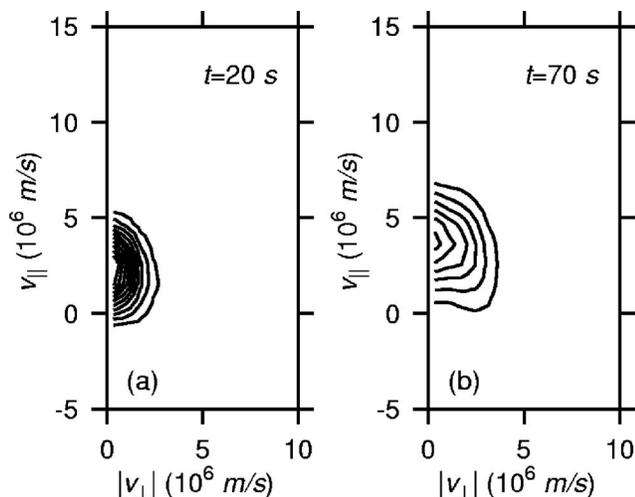

FIG. 5. (a) Distribution functions in Fig. 4(b) ($t=20$ s) plotted as a function of $|v_\perp|$ and $v_\parallel$. (b) Same, but for Fig. 4(d) ($t=70$ s). Contours are equally spaced in intervals of 5.

allel velocities (indicative of mirrored electrons travelling back up the field line). To first order, a possible explanation for this is that initially the current is being carried by electrons with mirror points well below the ionosphere (as these are the easiest to precipitate) which means there is little change in the perpendicular profile of the distribution function. However over time, the flux tube is depleted of these and electrons with mirror points at altitudes above the ionospheric boundary must be accelerated. Since the mirror force impedes the current carrying motions of the electrons in this case, more energy is required to accelerate them. This may have something to do with the saturation of the current in the hybrid model already noted in Fig. 3. Further study needs to be made of the dynamics of the current carrying electrons to clarify this point. This is particularly true for more realistic temperatures of a few hundred eV where nonlocal effects on the parallel electric field[22] (minimized here due to a lower temperature) are expected to be evident. Formations of distribution functions of similar nature have also been demonstrated in Vlasov simulations of electron acceleration by Alfvén wave pulses,[14] (including comparison with FAST data).

In Fig. 6, the situation along the magnetic field line corresponding to $x_2=0.1005$ is considered where the displayed quantity has been averaged with 5 grid lines to either side of $x_2=0.1005$. This was done to smooth out fluctuations evident as a function of x_2 in Fig. 3. Figure 6(a) displays the parallel current density. Due to the converging magnetic field geometry, the flux tube narrows as the ionospheric boundary is approached and the current density consequently increases. The increase in j_1 is proportional to B for $l_\parallel \gtrsim 6$ (since the total flux tube current is approximately constant here). Figure 6(b) illustrates the corresponding energy density along the same field line. The profile is steeper than for the current as the electron kinetic energy is $\propto v^2$ while the current density is $\propto v$. Figures 6(c) and 6(d) illustrate the distribution functions carrying the current at a distance of 10 R_E from the equator [dotted line in Fig. 6(a)] and at the northern ionospheric boundary, respectively. This reiterates the point made in Fig. 4 that the current is being carried by an increase in the drift of the distribution function. It also emphasizes the relative strength of the drift needed in the last couple of Earth radii before the ionospheric boundary to carry the required current. Contrasting Figs. 6(b) and 6(d), it is apparent that (for the parameters considered here at least) the majority of the electron kinetic energy is coming from this drifting of the distribution function while the slight approximately constant shift from zero in the electron energy density for $l_\parallel \lesssim 10$ [Fig. 6(b)] is due to the thermal energy.

Figure 7(a) contrasts the energy in u_3 and b_3 in both models. Focusing initially on the first quarter period (up to $t \approx 70$ s) of the MHD picture, the energy in the azimuthal velocity (which is the energy in the ion motion) decreases over time as it is converted into magnetic field energy. The decrease in u_3 energy in the hybrid picture is consistent with this as well, but there is a noticeable difference in the increase in magnetic field energy between the two models with less energy being put into the magnetic field in the hybrid case. The reason for this is evident in Fig. 7(b) where the
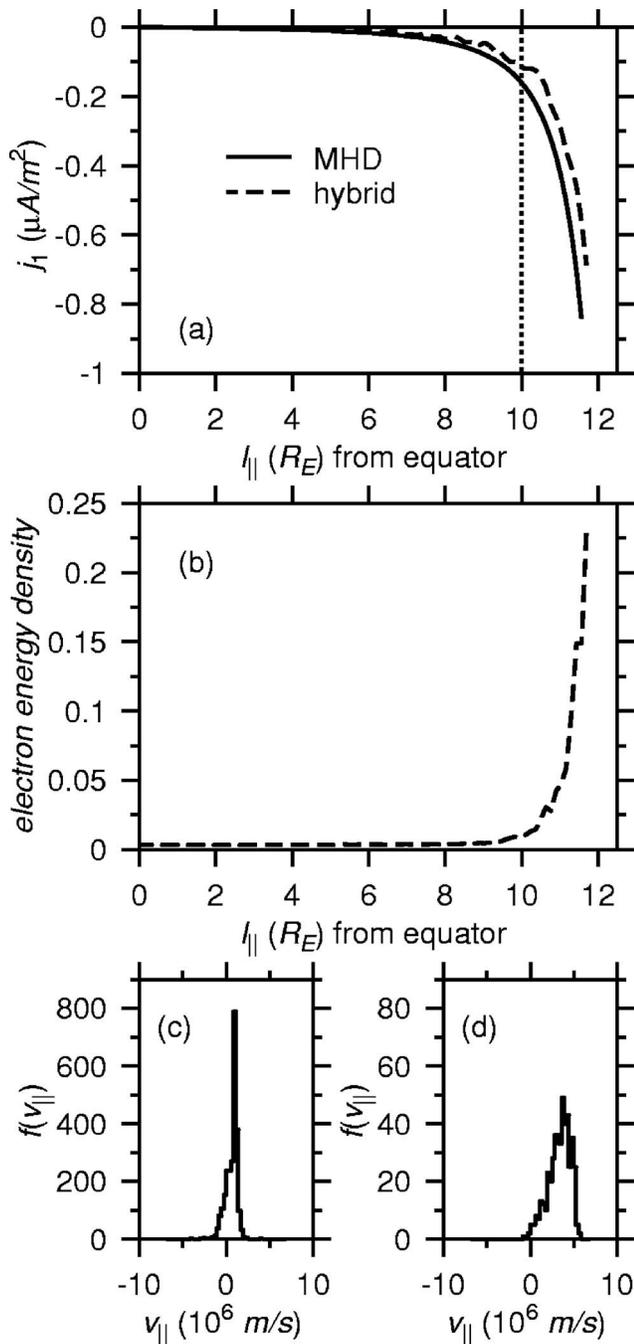
FIG. 6. (a) Parallel electron current density along $x_2 = 0.1005$ (at $t = 70$ s) as a function of distance along the field line (measured from the equator). (b) Same, but for electron energy density (hybrid model only). (c) Distribution function at $l_\parallel = 10$ R_E [refer to dashed line in panel (a)]. (d) Distribution function at the ionospheric boundary. The distribution functions in (c) and (d) are compiled for the same range in x_2 as noted in Fig. 4 [and thus Figs. 4(d) and 6(d) are the same data].
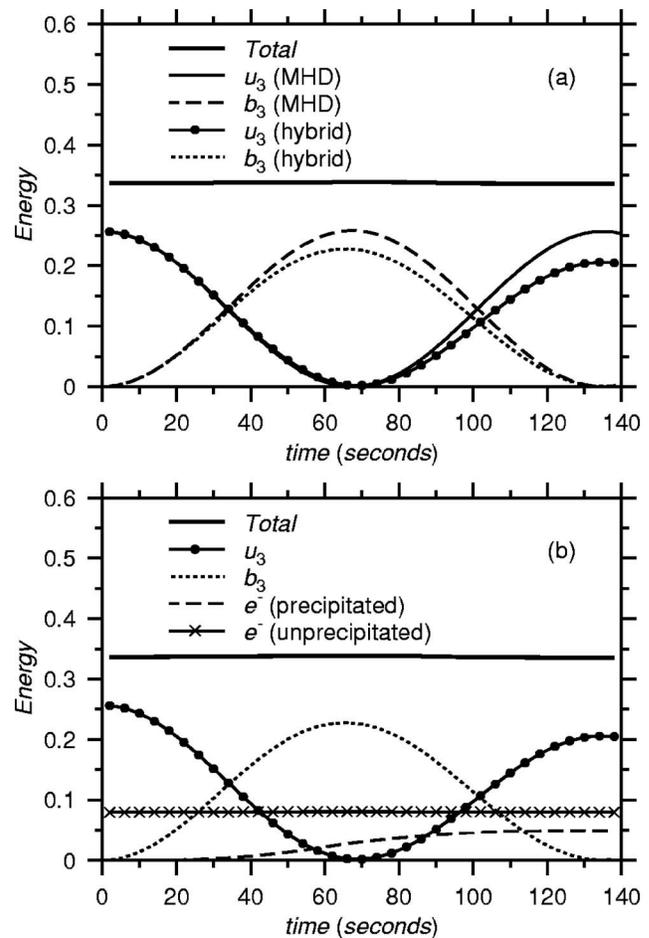

FIG. 7. (a) The energy in the azimuthal velocity, u_3 and azimuthal magnetic field b_3 from the hybrid model (as a function of time for half an Alfvén period) contrasted with the same from the cold plasma MHD model. (b) Total and component energies for the hybrid model.

components of energy in the hybrid model are displayed. The energy in the precipitated electron population increases along with the magnetic energy as electrons are accelerated to carry the current. Therefore, a portion of the ion kinetic energy is being converted into electron kinetic energy resulting in less being transferred into magnetic field energy. Since these electrons leave the simulation domain, they represent a net loss of shear Alfvén wave energy. The fact that the energy in the unprecipitated electron population remains essentially unchanged though illustrates that the percentage of electrons precipitated is actually very small.

During the second quarter cycle, the situation becomes reversed. Magnetic field energy is now being converted back into ion kinetic energy. However, a portion of this energy is still being transferred into the electrons to carry the decreasing, but still upward, field aligned current. Since the current is decreasing, the rate of increase of the energy of the precipitated electron population gradually decreases and drops to zero by the half cycle. At this point, there is a net difference of about 20% between the u_3 energy in the hybrid and MHD models. This is equal to the total amount of Alfvén wave energy lost to the electrons over the entire upward current phase interval. During the following downward current phase, ionospheric electrons would be accelerated up the field lines to carry the current, but this energy would come from the Alfvén wave as well and so would represent a similar drain on Alfvén wave energy.

The percent change in total energy over the length of the run was less than a percent and results were consistent with an additional run done with double the number of simulation electrons. A convergence test was performed between the two runs using the azimuthal magnetic field data (b_3) at a

quarter period ($t = 70$ s, where the field attains its maximum value) using the definition

$$\frac{\Sigma_i |b'_{3_i} - b_{3_i}|}{\Sigma_i |b'_{3_i} + b_{3_i}|/2}$$

where the prime denotes the run with double the particle resolution and the summation is over all the grid points. It was found that the error in the fields by this measure was about 4%.

The analysis thus far has only considered the case of $\lambda_{\perp_{eq}} = 0.25 \, R_E$. Figure 8(a) displays the energy lost from the Alfvén wave through electron precipitation after 1/2 cycle for 3 equatorial widths from 0.15 R_E to 0.5 R_E. As would be expected, this energy dissipation increases significantly as the flux tube narrows. The nonlinear increase is to be expected since the energy loss rate $\propto v_1^3$ and $v_1 \propto 1/\lambda_\perp$. Figures 8(b) and 8(c) display the current densities at $t = 70$ s for the two limits of $\lambda_{\perp_{eq}} = 0.5 \, R_E$ and $\lambda_{\perp_{eq}} = 0.15 \, R_E$, respectively, along with the current from the MHD models. In the former case, as would be expected, the two models agree very well. In the latter, the divergence between the two is even stronger than for $\lambda_{\perp_{eq}} = 0.25 \, R_E$ along with what appears to be a pronounced widening of the perturbation. Even though there is the stronger divergence from MHD, which is expected since greater electron acceleration is required for a narrower flux tube, it is interesting to note that the saturated current in the hybrid case is of a similar magnitude to the $\lambda_{\perp_{eq}} = 0.25 \, R_E$ case. One possible interpretation is that as it becomes more difficult to accelerate electrons to carry the total current through the initial flux tube, electrons along the field lines adjacent to this are in-turn accelerated so that the total current across the new wider flux tube is similar to that which passes through the original flux tube in the MHD picture. They are not expected to be identical as the dissipation of energy in the hybrid picture also changes the characteristic of the current profile.

The peak drifts in the distribution function between about $t = 50$ and $t = 60$ s for the case of $\lambda_{eq_\perp} = 0.15 \, R_E$ is about 150 eV. From Ref. 9, the ratio of the energy expended through electron acceleration (ξ_e) to joule heating (ξ_j) is given by

$$\frac{\xi_e}{\xi_j} = \frac{1}{2} \mu_o \Sigma_p v_d \left(\frac{\lambda_e}{\lambda_\perp} \right)^2, \tag{9}$$

where Σ_p is the height integrated Pedersen conductivity, v_d is the drift velocity of the current carrying electron beam. From Fig. 8(b), it is evident that the half-wavelength $\lambda/2 \approx 2\pi\lambda_e$. Therefore $\lambda_\perp/\lambda_e \approx 4\pi$. Choosing $\Sigma_p = 10$ mhos (Siemens), the energy ratio is $\xi_e/\xi_j = 0.3$. Therefore for these values, energy loss due to electron energization and precipitation in the ionosphere would account for about 30% of the total energy dissipated with the other 70% being lost to Joule heating in the ionosphere. For much narrower scale lengths, it is then expected that the dissipation due to electron acceleration would dominate that due to Joule heating. This is confirmed in the observations in Ref. 8, where they noted an up to an order of magnitude increase between electron energies between Cluster and FAST altitudes (proportional to the
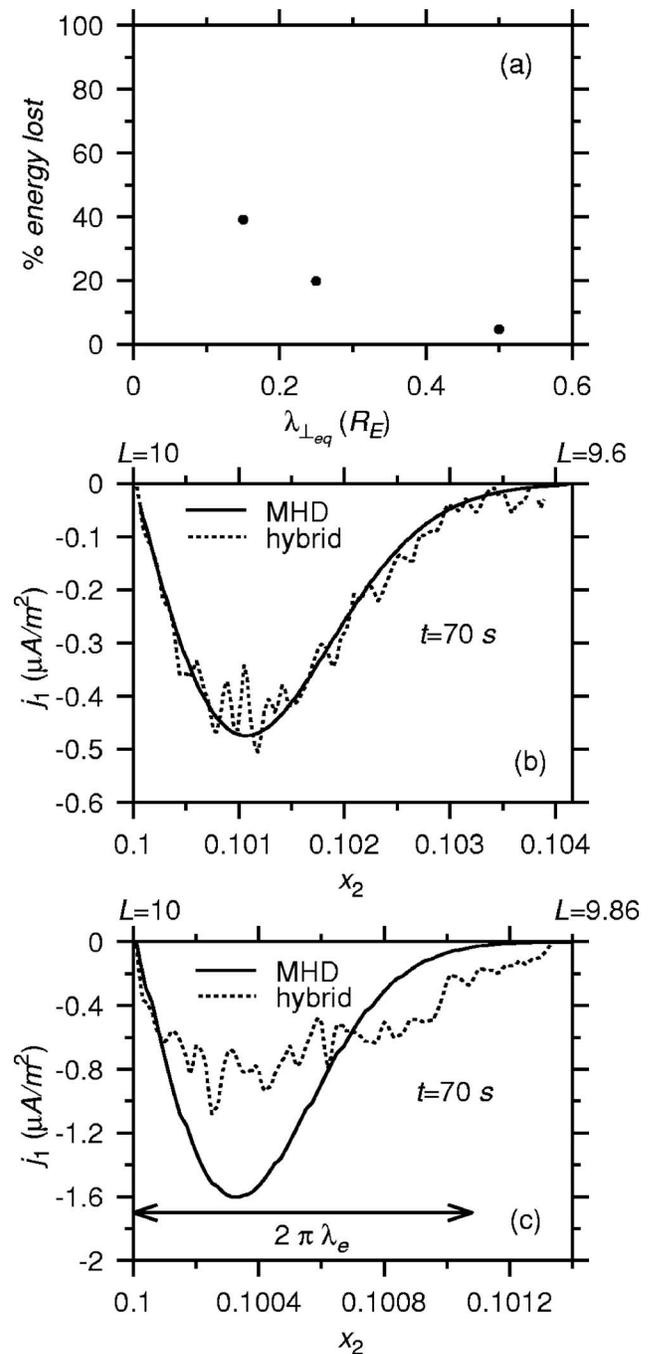

FIG. 8. (a) Alfvén wave energy lost at 1/2 Alfvén period as a function of initial equatorial width, $\lambda_{\perp_{eq}}$ ($\lambda_{\perp_{eq}} = 0.25 \, R_E$ is the case presented in the preceding figures). (b) Same as Fig. 3(c), but for $\lambda_{\perp_{eq}} = 0.5 \, R_E$. (c) Same, but for $\lambda_{\perp_{eq}} = 0.15 \, R_E$.

decrease in Poynting flux between the two spacecraft) for perpendicular wavelengths on the order of the electron inertial length (inertial shear Alfvén waves) and ion gyroradius (kinetic Alfvén waves). Many of these waves were observed to occur along open magnetic field lines and so were not necessarily associated with FLRs, but it serves to stress the point already made here. In the MHD theory of FLRs, it is possible for them to phase mix down to perpendicular length scales on the order of $2\pi\lambda_e$ but we have not considered that limit in this paper since the energy description starts to be-

come somewhat modified from what we have presented here and this will be discussed more in a future publication. Also, between the energy lost to electron acceleration and Ohmic dissipation, it is not clear that many resonance systems narrowing due to phase mixing would reach perpendicular widths much less than already considered before being totally dissipated.

In addition to the dissipation noted here, energy can be taken from Alfvén waves via resonant wave-particle interactions (Landau damping) when v_{th} is on the order of the phase velocity of the wave (where $v_{ph} \sim V_A$ for $k_\perp \lambda_e \ll 1$). This was the subject of a dispersion relation study in Ref. 23 and a numerical study in Ref. 16 with a box version of the hybrid code used here. However, since most of the electron acceleration is happening close to the ionosphere where $v_{th} \ll V_A$, Ref. 23 noted that flux tube widths would have to be on the order of a km for Landau damping effects to be significant. Since the minimum flux tube width we consider is on the order of $4\pi\lambda_e \approx 66$ km, Landau damping effects will be of negligible importance to the results quoted here.

As a final point, it is instructive to look at the structure of the parallel electric field associated with the electron acceleration. There is some degree of numerical noise associated with displaying the instantaneous field which can be removed by time averaging over a specified interval and then spatially averaging over adjacent grid points (using the $1/4 -1/2-1/4$ weighting mentioned previously). This is a common diagnostic technique in particle-in-cell simulations. Figure 9 illustrates the unaveraged parallel current [Fig. 9(a)] and time averaged (over a 5 s interval) parallel electric field along the field line at $x_2=0.1003$ at several times for $\lambda_{\perp eq} =0.15\ R_E$. Consistent with Fig. 6(a), the parallel current has the strongest increase in the last two Earth radii above the ionospheric boundary and the current is beginning to saturate as t increases. In order to facilitate the acceleration of the electrons to carry the current, the parallel electric field has a similar profile with magnitudes of a few hundredths of mV/m supporting field aligned currents of several tenths of $\mu A/m^2$ close to the ionospheric boundary.

IV. CONCLUSIONS

We have used a 2D hybrid MHD-kinetic model to study the electron response to a fundamental mode shear Alfvén wave velocity perturbation centered on an $L=10$ magnetic field line for half of an Alfvén period. A half-Gaussian was chosen for the perpendicular profile of the initial velocity perturbation so that only the case of upward field aligned currents corresponding to downwelling electrons was considered. The field aligned profile of the eigenmode along the field line was adapted from the profile used in Ref. 9, based on the analytical model of Ref. 20. For a maximum equatorial velocity perturbation of 100 km/s, number density of 10^6 m^{-3}, and an equatorial perpendicular wavelength of 0.25 R_E, a maximum field aligned current of $\sim 0.7\ \mu A/m^2$ was produced at the ionospheric boundary carried by an electron beam with energy ~ 70 eV. The majority of the acceleration occurred in the final 2 R_E above the ionospheric boundary (corresponding to the region of largest magnetic field curva-
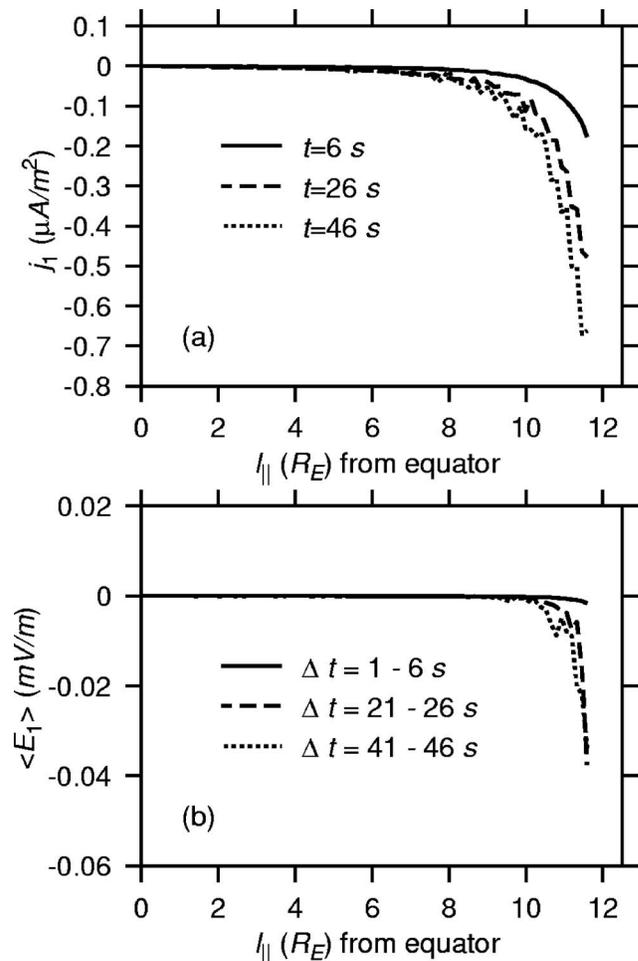

FIG. 9. (a) Parallel current density along $x_2=0.1003$ as a function of distance along the field line (measured from the equator). (b) Same, but for time averaged parallel electric field (averaged over the 5 s intervals indicated).

ture) and the energy used to accelerate the electrons dissipated about 20% of the total Alfvén wave energy by a half period.

As expected for narrower Alfvén waves, the dissipation was stronger as electrons must be accelerated more to carry the required current culminating in a loss of wave energy $\sim 40\%$ for the equatorial $\lambda_{\perp eq} =0.15\ R_E$ over a half cycle. Using the results from the two fluid analysis in Ref. 9, it was illustrated in this case that energy dissipated by electron acceleration was expected to be on the same order as ionospheric Ohmic dissipation. Therefore, even for the case of infinite conductivity, a FLR could be effectively damped over a few cycles by electron acceleration alone.

In summary then, for initial FLR equatorial widths greater than about 0.5 R_E, very little energy is dissipated in the acceleration of electrons, but this will increase nonlinearly as the resonance narrows due to phase mixing effects. By the time this narrowing reaches equatorial widths <0.2 R_E most of the wave energy, unless the system is driven, would be damped in a couple of cycles.

As previously mentioned, the thermal temperature of the distribution function used in this study is lower than actually observed. This was done in order to concentrate on under-

standing the simpler system initially in the absence of stronger mirror force effects. However, as mirror force effects would only impede electron motion along the field line, the simulations here can be seen to be indicative of a lower limit to the energy dissipation that might be expected for higher temperatures. In addition, the model is only two-dimensional, but since FLR systems can extend for hundreds of kilometers in the azimuthal direction, it is a very good first order approximation for studying the field aligned acceleration in such systems.

ACKNOWLEDGMENTS

APPENDIX A: PARTICLE INITIALIZATION AND PIC TECHNIQUE

The positions of the particles are assigned such that initially n_{1p} particle positions are chosen in the field aligned direction and n_{2p} in the perpendicular direction yielding a total number of particles given by $n_p = n_{1p} n_{2p}$. The field aligned positions are initialized so that $\int h_1 h_2 h_3 dx_1$ is constant along the field line in the center of the simulation grid and the n_{2p} positions in the perpendicular direction are assigned equally spaced in x_2. This yields an essentially constant density throughout the simulation domain.

The moments of the particle distribution function are compiled at the grid points using PIC techniques (discussed in Ref. 21) where the first two moments

$$n_e = \int f d^3 v = \sum_i S(\vec{x}, \vec{x}_i), \tag{A1}$$

$$j_e = -e \int v_1 f d^3 v = -e \sum_i v_{1_i} S(\vec{x}, \vec{x}_i) \tag{A2}$$

are electron number density and current density, respectively, and $S(\vec{x}, \vec{x}_i)$ is the particle shape function which discretizes the electron information (charge, velocity, etc.) to the grid point. This latter takes the form of a bilinear routine which breaks up each grid cell into four subcells defined by the position of the ith electron in the summation (see Fig. 10). The nonuniformity of the dipolar grid made it difficult to assign subareas accurately and efficiently and so the following approximation was used. In Fig. 10, the length and width of subcell b are determined, respectively, by

$$L_b \approx \tfrac{1}{2}(h_1^e + h_1^D)|(x_1^{DC} - x_1^e)|,$$

$$w_b \approx \tfrac{1}{2}(h_2^D + h_2^e)|(x_2^{DA} - x_2^e)|,$$

where the superscript e refers to the electron and x_1^{DC} is the value of x_1 along the arc between points D and C. The area
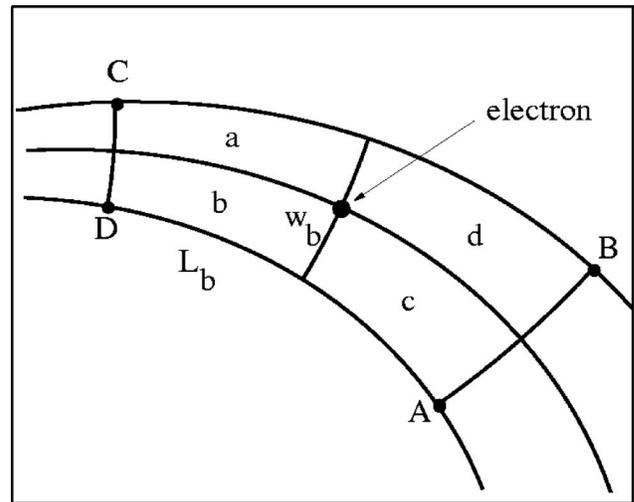

FIG. 10. Example of modified bilinear interpolation scheme in dipolar coordinates. L_b is the approximate length along x_1 and w_b the approximate width in the x_2 direction of subcell b (from Ref. 18).

of subcell A_b is then given simply by the product $L_b w_b$ and the portion of the electron's properties (e.g., parallel velocity v_1) assigned to point B is determined from

$$\frac{A_b}{(A_a + A_b + A_c + A_d)} v_1$$

where the other subcell areas are similarly determined. This is in-turn divided by the volume of each grid cell (having unit length in the invariant direction x_3) given by $(A_a + A_b + A_c + A_d) h_{3_B}$ where h_3, with units of length, accounts for the azimuthal variation of the flux tube along the field line. The area weights are also used to assign the forces (electric and magnetic field values) to the particle positions and so the interpolation of field value F to particle position is given by

$$F(\vec{x}_1) = \frac{A_a F(\vec{x}_A) + A_b F(\vec{x}_B) + A_c F(\vec{x}_C) + A_d F(\vec{x}_D)}{A_a + A_b + A_c + A_d}.$$

Each simulation electron is a "superparticle" representative of many electrons and the scaling is done using a ratio of the constant number density from the fluid $n_o = \rho_o / m_p$ so that the final expression for the electron number density and current density are given by

$$n_e(\vec{x}) = \frac{n_o(\vec{x})}{n_{e_o}} \sum_i S(\vec{x}, \vec{x}_i),$$

$$j_e(\vec{x}) = -e \frac{n_o(\vec{x})}{n_{e_o}} \sum_i v_i S(\vec{x}, \vec{x}_i),$$

where $n_{e_o} = \sum_i S(\vec{x}, \vec{x}', t=0)$. This also allows any irregularities in n_{e_o} due to positioning to be absorbed into the scaling ratio so the resulting number density is constant.

APPENDIX B: PARALLEL ELECTRIC FIELD

From Ampere's law, the expression for the field aligned current density is given by

$$\mu_o j_1 = \frac{1}{h_2 h_3} \frac{\partial}{\partial x_2}(h_3 b_3), \tag{B1}$$

where $b_2 = 0$ has been used. Taking the time derivative

$$\mu_o \frac{\partial j_1}{\partial t} = \frac{1}{h_2 h_3} \frac{\partial}{\partial x_2}\left(h_3 \frac{\partial b_3}{\partial t}\right) \tag{B2}$$

and substituting in for $\partial b_3 / \partial t$ from Faraday's law yields

$$\mu_o \frac{\partial j_1}{\partial t} = -\frac{1}{h_2 h_3} \frac{\partial}{\partial x_2}\left(\frac{h_3}{h_1 h_2}\frac{\partial}{\partial x_1}(h_2 E_2)\right)$$
$$+ \frac{1}{h_2 h_3} \frac{\partial}{\partial x_2}\left(\frac{h_3}{h_1 h_2}\frac{\partial}{\partial x_2}(h_1 E_1)\right). \tag{B3}$$

The gyroaveraged Vlasov equation (e.g. Ref. [24]) is given by

$$\frac{df}{dt} = \frac{\partial f}{\partial t} + \frac{dx_1}{dt}\frac{\partial f}{\partial x_1} + \frac{dv_1}{dt}\frac{\partial f}{\partial v_1} + \frac{dv_\perp}{dt}\frac{\partial f}{\partial v_\perp} = 0 \tag{B4}$$

and conservation of magnetic moment yields

$$\frac{dv_\perp}{dt} = \frac{v_1 v_\perp}{2 B_o}\frac{1}{h_1}\frac{\partial B_o}{\partial x_1}, \tag{B5}$$

where B_o is the ambient magnetic field. Using this and the equation of motion (3) to substitute in for $dv_\perp/dt$ and dv_1/dt, respectively, in the Vlasov equation gives

$$\frac{df}{dt} = \frac{\partial f}{\partial t} + \frac{v_1}{h_1}\frac{\partial f}{\partial x_1} + \left(-\frac{e}{m_e}E_1 - \frac{\mu_m}{m_e}\frac{1}{h_1}\frac{\partial B_o}{\partial x_1}\right)\frac{\partial f}{\partial v_1}$$
$$+ \left(\frac{v_1 v_\perp}{2 B_o}\frac{1}{h_1}\frac{\partial B_o}{\partial x_1}\right)\frac{\partial f}{\partial v_\perp} = 0, \tag{B6}$$

where (4) has been used as well. Multiplying by $-e v_1$ and then integrating over velocity space results in a second expression for $\partial j_1 / \partial t$,

$$\frac{\partial j_1}{\partial t} = \frac{e}{h_1}\frac{\partial}{\partial x_1}\int v_1^2 f d^3 v + \frac{ne^2 E_1}{m_e} + \frac{e}{m_e}\frac{1}{h_1}\frac{\partial B_o}{\partial x_1}\int \mu_m f d^3 v$$
$$- \frac{e}{m_e}\frac{2}{h_1}\frac{\partial B_o}{\partial x_1}\int \frac{m_e v_1^2}{2 B_o} f d^3 v, \tag{B7}$$

where the definitions $j_1 = -e\int v_1 f d^3 v$ and $n = \int f d^3 v$ have been used. Equating (B3) and (B7) then yields the final expression for the parallel electric field

$$\frac{\partial}{\partial x_2}\left(\frac{h_3}{h_1 h_2}\left(\frac{\partial G}{\partial x_2}\right)\right) - \frac{G}{\lambda_e^2}$$
$$= \frac{\partial}{\partial x_2}\left(\frac{h_3}{h_1 h_2}\frac{\partial}{\partial x_1}(h_2 E_2)\right) + e\mu_o \frac{\partial}{\partial x_1}\int v_1^2 f d^3 v$$
$$+ \mu_o \frac{e}{m_e}\frac{\partial B_o}{\partial x_1}\int \mu_m f d^3 v - 2\mu_o \frac{e}{m_e}\frac{\partial B_o}{\partial x_1}\int \frac{m_e v_1^2}{2 B_o} f d^3 v, \tag{B8}$$

where $G = h_1 E_1$. The second term on the right-hand side relates to the field aligned gradient of the parallel electron pressure while the last two terms are due to the perpendicular and parallel electron pressures, respectively. They are in balance when the plasma is isotropic (see Ref. [25] for a lucid discussion). These last three terms are computed using the same basic procedure as outlined for electron number and current density in Appendix A (i.e., integrals over f becomes summations of the particle shape function, S).

APPENDIX C: ENERGY INVARIANT

Following Ref. [17], the energy invariant for the system (understood as an energy per unit of the azimuthal coordinate, x_3)

$$T_E = \int_A h_1 h_2 h_3 dx_1 dx_2 \frac{\rho_o u_3^2}{2} + \int_A h_1 h_2 h_3 dx_1 dx_2 \frac{b_3^2}{2}$$
$$+ \frac{C}{2}\sum_i v_i^2 + \frac{C}{2}\sum_i v_{i_p}^2, \tag{C1}$$

where $C = m_e/m_p \int h_1 h_2 h_3 dx_1 dx_2 n_o / n_p$ is a constant and the subscript i_p denotes electrons that have been precipitated, whereas i denotes electrons that are still in the simulation domain. The Poynting flux term vanishes since there are nodes of E_2 at the ionospheres.

[1] B. L. Xu, J. C. Samson, W. W. Liu, F. Creutzberg, and T. J. Hughes, J. Geophys. Res. **98**, 11531 (1993).
[2] W. Lotko, A. V. Streltsov, and C. W. Carlson, Geophys. Res. Lett. **25**, 4449 (1998).
[3] J. C. Samson, R. Rankin, and V. T. Tikhonchuk, Ann. Geophys. **21**, 933 (2003).
[4] R. S. Newton, D. J. Southwood, and W. J. Hughes, Planet. Space Sci. **26**, 201 (1978).
[5] W. Allan and F. B. Knox, Planet. Space Sci. **27**, 79 (1979).
[6] W. Allan and A. N. Wright, J. Geophys. Res. **102**, 19927 (1997).
[7] C. C. Chaston, J. W. Bonnell, L. M. Peticolas, C. W. Carlson, J. P. McFadden, and R. E. Ergun, Geophys. Res. Lett. **29**, 1535 (2002).
[8] C. C. Chaston, L. M. Peticolas, C. W. Carlson, J. P. McFadden, F. Mozer, M. Wilber, G. K. Parks, A. Hull, R. E. Ergun, R. J. Strangeway, M. Andre, Y. Khotyaintsev, M. L. Goldstein, M. Acuña, E. J. Lund, H. Reme, I. Dandouras, A. N. Fazakerley, and A. Balogh, J. Geophys. Res. **110**, A02211 (2005).
[9] A. N. Wright, W. Allan, and P. A. Damiano, Geophys. Res. Lett. **30**, 1847 (2003).
[10] I. R. Mann, A. N. Wright, and P. S. Cally, J. Geophys. Res. **100**, 19441 (1995).
[11] C. H. Hui and C. E. Seyler, J. Geophys. Res. **97**, 3953 (1992).
[12] C. E. J. Watt, R. Rankin, and R. Marchand, Phys. Plasmas **11**, 1277 (2004).
[13] C. E. J. Watt, R. Rankin, I. J. Rae, and D. M. Wright, J. Geophys. Res. **110**, A10S07 (2005).
[14] C. E. J. Watt, R. Rankin, I. J. Rae, and D. M. Wright, Geophys. Res. Lett. **33**, L02106 (2006).
[15] P. A. Damiano and A. N. Wright, J. Geophys. Res. **110**, A01201 (2005).
[16] P. A. Damiano, R. D. Sydora, and J. C. Samson, J. Plasma Phys. **69**, 277 (2003).
[17] P. A. Damiano, A. N. Wright, R. D. Sydora, and J. C. Samson, Phys. Plasmas **12**, 042105 (2005).
[18] P. Damiano, Ph.D. thesis, University of Alberta (2002).
[19] A. N. Wright, W. Allan, M. S. Ruderman, and R. C. Elphic, J. Geophys. Res. **107**, 1120 (2002).

[20]J. P. H. Taylor and A. D. M. Walker, Planet. Space Sci. **32**, 1119 (1984).

[21]C. K. Birdsall and A. B. Langdon, *Plasma Physics Via Computer Simulation* (McGraw-Hill, New York, 1985).

[22]R. Rankin, J. C. Samson, and V. T. Tikhonchuk, Geophys. Res. Lett. **26**, 3601 (1999).

[23]R. Lysak and W. Lotko, J. Geophys. Res. **101**, 5085 (1996).

[24]K. Rönnmark, J. Geophys. Res. **107**, 1430 (2002).

[25]R. H. Comfort, in *Geophysical Monograph 44: Modeling Magnetospheric Plasma*, edited by T. Moore and J. W. Jr. (American Geophysical Union, Washington, D.C., 1988), pp. 51–53.